ONERA Three-Dimensional Icing Model

T. Hedde* and D. Guffond*

ONERA, Châtillon Cedex 92322, France

A three-dimensional icing model has been developed at ONERA to calculate ice accretion shapes for aerodynamic components that can not be predicted using conventional two-dimensional codes. It is described, emphasizing the original parts with respect to the two-dimensional existing models. The model includes Euler inviscid flow calculation. Droplet trajectories are calculated in a three-dimensional grid. The remesh on the leading edge is adapted to follow aerodynamics singularities. The boundary layer is calculated using a mixing length formulation to model the wall roughness influence on convective heat transfer. Runback paths are integrated. The heat balance is calculated in a grid created along the runback paths. The domain of validity of the three-dimensional icing code is described; compared with the two-dimensional model this domain is wider, especially for high speeds. The three-dimensional model is shown to simulate well a uniform ice deposit on a three-dimensional rotor blade tip. Then, a comparison of the three- and two-dimensional codes on an infinite swept wing shows that the corrected two-dimensional code predicts the catch efficiency but not the ice shape. Finally, it is shown that the continuum flux hypothesis prevents the three-dimensional model from simulating correctly the "lobster tail" ice shape (nonuniform ice deposit).

Nomenclature

C	= chord, m
F	= turbulence damping factor
f	= volumetric forces in running back water, N/m^3
h	= heat transfer coefficient, W/Km^2
hf	= water film height, m
ht	= ice height, m
k_{max}	= maximum roughness height, m
ks	= sand grain equivalent roughness, m
LWC	= liquid water content in the freestream, kg/m^3
l_m	= mixing length, m
Mm	= molar mass, kg/mole
$\dot{m}$	= mass flux surface density, kg/m$^2 \cdot$ s
P	= pressure, Pa
P_{VS}	= vapor partial pressure, Pa
R	= streamlines curvature radius, m
S	= surface, m^2
s	= curvilinear abscissa along streamlines, m
$U(y)$	= boundary-layer velocity, air, m/s
U_∞	= freestream velocity, m/s
u	= running back water velocity vector, m/s
T_r	= recovery temperature, K
T_W	= wall temperature, K
T_∞	= freestream temperature, K
w	= component of water speed perpendicular to the streamlines, m/s
X, Z	= nondimensional coordinates of the body wall, profile direction and span direction, respectively
y	= distance to the wall, m
β	= local catch efficiency
β_0	= wall streamlines direction, rad
Δt	= icing or impact duration, s
δ	= boundary-layer thickness, m
ν	= kinematic viscosity, m^2/s
ρ	= volumetric mass, kg/m^3
τ_t	= turbulent shearing stress, N/m^2
τ_0	= wall shearing stress, N/m^2

Subscripts

∞	= in the freestream region
i	= impingement or cell indices
r	= transverse to the streamlines
w	= wall
vap	= evaporation, sublimation

Introduction

ICING is a meteorological hazard that may affect aircraft and helicopter operations due to supercooled droplets that impinge on the front parts of the different structures. The impinging water freezes, and the ice deposit produces very high-aerodynamic degradation. Manufacturers have to demonstrate that their aircraft can fly in icing conditions. This may be achieved by flight tests or modeling. As flight tests are expensive and the icing conditions obtained during the tests are not always as severe as required, computer models are often used to determine the ice shape deposit in failure cases and on the unprotected parts of the aircraft. The computed shapes are then reproduced and applied to a real aircraft in order to justify the absence of protection and/or analyze the aircraft behavior when the existing protection is out of order. Two-dimensional and three-dimensional icing models have been developed at ONERA as well as in other countries.

The first two-dimensional icing model was developed to calculate ice growth on wings; later a three-dimensional icing model[1,2] was developed in order to have a tool for calculating ice accretion shapes on such profiles as finite swept wings, aircraft noses, or air intakes. The two-dimensional icing code cannot be used for such shapes. This paper presents the hypotheses used by ONERA in three-dimensional modeling, with emphasis on the differences between the two- and three-dimensional codes. Comparisons with experimental shape will be done as well.

The three-dimensional icing model is built on the following frame (Fig. 1) which is basically (except for step 4) the same as in the two-dimensional icing model[3]: 1) inviscid fluid flowfield calculation, 2) droplet trajectories and local catch efficiency, 3) boundary layer on a rough surface, 4) runback paths calculation, and 5) heat balance and ice height.

In a three-dimensional icing model a crucial problem is to make the grid fit the physical reality. Each step of the model requires a specific optimization of the body grid; this leads to the definition of five successive grids called 1) geometric grid, 2) collection grid, 3) aerodynamic grid, 4) thermodynamic grid, and 5) iced body grid.

Inviscid Flow (Geometric Grid)

The inviscid fluid flowfield calculation may either be calculated with a panel method (compressibility correction up to Mach 0.5)
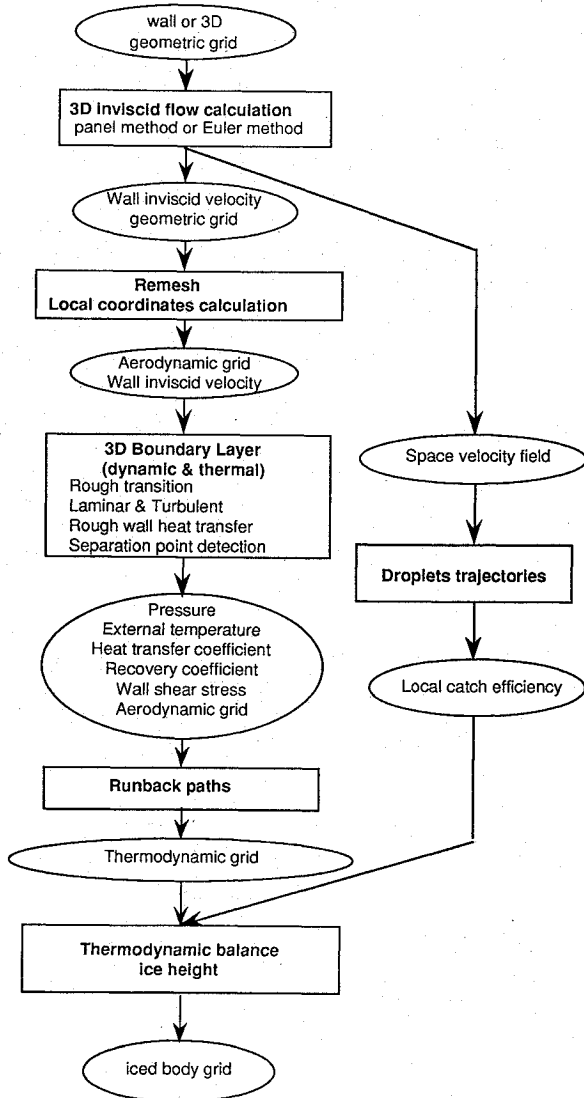
Fig. 1   Three-dimensional icing model structure.

Fig. 2   Calculation of a value of the local catch efficiency β, projection of surface elements ΔS_{∞} along the droplet trajectory lines on the body wall defines a new partial grid of the body (collection grid) defined by the surface elements ΔS_i.

Fig. 3   Separation line body (airfoil), X is curvilinear abscissa along the profile and Z is span direction. If the boundary layer had to be calculated in a) the geometric grid a large region around the stagnation line would not be calculable; on the contrary, b) the aerodynamic grid enables the boundary-layer calculation to start close to stagnation line.

or with an Euler method (valid in the subsonic and transonic domains). An additional advantage of the Euler method is that it is fully compressible.

Three-Dimensional Trajectories Calculation (Collection Grid)

The droplet trajectories are calculated assuming the aerodynamic drag is the only force affecting droplet motion. This calculation requires the knowledge of local velocity in all of space. As the Euler method gives the velocity field at each node of a three-dimensional grid in the space around the body, a triple linear interpolation allows the calculation of the velocity anywhere inside a cell. Hence, the impact positions of four trajectories are determined enabling the calculation of the local catch efficiency β, which is defined as the fraction of the freestream water concentration that is incident at a particular surface location (equal to the ratio of a freestream surface ΔS_{∞} to the projection of the same surface, along a trajectory tube, on the body wall ΔS_i) (see Fig. 2). Values of β are, therefore, spread anywhere on the body wall at the center of each surface element ΔS_i. This defines a new grid on the body (collection grid). Therefore, an interpolation of β has to be done to obtain value of β in each cell of the grid (thermodynamic grid) used to establish the thermodynamic balance.

Aerodynamic Grid Creation

The inviscid flow is calculated in the geometric grid that has to be built with similar size panels. Because of the fact that the ice generally grows close to the stagnation line (on a wing), the grid
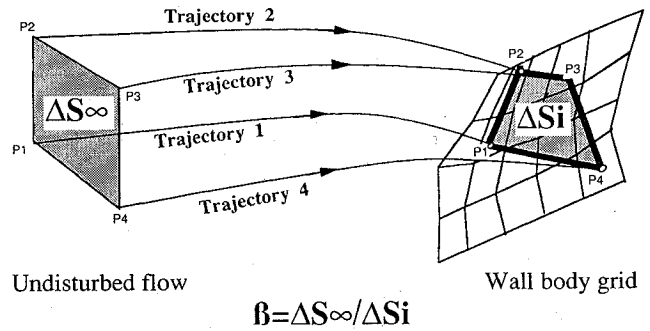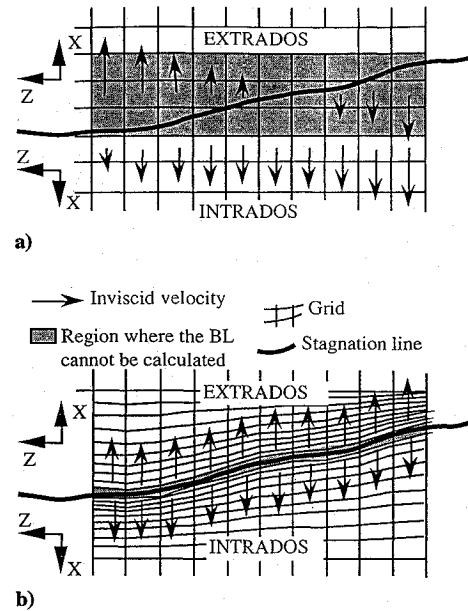
has to be denser in this region. Moreover, to improve the boundary-layer calculation near the stagnation line, the grid singularities (grid lines) have to follow the flow singularity (stagnation line). Then, a new grid, called the aerodynamic grid, is built to take into account these constraints (Figs. 3 and 4).

Boundary-Layer Calculation (Roughness Model)

The three-dimensional boundary layer is calculated in the aerodynamic grid. This allows the calculation of the boundary-layer characteristics as close as wanted to the flow singularities (stagnation line or stagnation point). The outputs are the heat transfer coefficient on a rough wall h, the wall stream direction β_0, and the wall shear stress value τ_0.

The boundary-layer code (finite volumes) used in the three-dimensional icing code was originally developed for smooth wall calculations.[4] It was, therefore, necessary to develop a rough wall model for simulating the iced wall effect on the boundary layer.

The transition caused by roughness is detected classically by the mean of a local Reynolds number based on the roughness maximum height. The transition criterion is

$$Re(k_{max}) = \left[\frac{U(y) \cdot y}{v(y)} \right]_{(y = k_{max})} > 600 \qquad (1)$$

a) Geometric grid

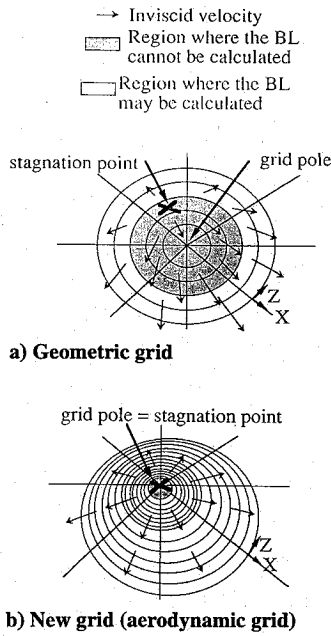b) New grid (aerodynamic grid)

Fig. 4 Stagnation point body, nose, grid pole moved to be coincident with the stagnation point permitting boundary-layer calculation to start as close as wanted to the pole.

The increase of the convection heat transfer, due to the roughness in the turbulent region, is modeled by an increase of the smooth wall turbulent shear stress (Van Driest formulation[5]). The turbulent shear stress may be expressed by use of the mixing length formulation

$$\tau_t = \rho \cdot F^2 \cdot l_m^2 \cdot \left[\left(\frac{\partial u}{\partial y} \right)^2 + \left(\frac{\partial w}{\partial y} \right)^2 \right] \qquad (2)$$

where the mixing length after Michel et al.[6] is

$$l_m = \delta \cdot \kappa_r \cdot \tanh\left(\frac{\kappa}{\kappa_r} \frac{y}{\delta} \right) \qquad (3)$$

with $\kappa_r = 0.085$ and $\kappa = 0.41$ and

$$F = 1 - \exp\left(\frac{l_m\sqrt{\tau \cdot \rho}}{26 \cdot \kappa \cdot \mu} \right) \qquad (4)$$

where F is the turbulence damping factor near a smooth wall.

The roughness effect is simulated by modifying F so as to annihilate its damping effect and increase the turbulent shear stress. Using the Van Driest roughness model F then becomes

$$F = 1 - \exp\left(\frac{l_m\sqrt{\tau \cdot \rho}}{26 \cdot \kappa \cdot \mu} \right) + \exp\left(\frac{60 \cdot y}{26 \cdot k_s} \right) \qquad (5)$$

where k_s is the equivalent sand grain roughness.

This new calculation of the mixing length is injected in the boundary-layer code to obtain the thermal structure of the boundary layer. Then the heat transfer coefficient h is calculated as

$$h = \lambda \cdot \left(\frac{\partial T}{\partial y} \right)_{y=0} \bigg/ (T_w - T_r) \qquad (6)$$

Because of the lack of experimental knowledge about ice roughness,[7,8] a uniform roughness is used in the three-dimensional model, $k_s/C = 10^{-3}$. Nevertheless, the three-dimensional model may accept one roughness height definition per grid cell.

Runback Paths

In a three-dimensional icing model, running back of water occurs on a surface; thus, unlike two-dimensional icing models, it is necessary to calculate the runback paths along the body wall. Knowing these paths enables one to determine where the running back water freezes.

For aircraft speed the air/water interface friction is the main runback driving force. It is thought that running back water closely follows the wall air streamlines. To check this hypothesis and the validity range of such an assumption the deviation of the water runback from wall air streamlines direction has to be quantified.

Deviation of the Runback with Respect to the Wall Air Streamlines

The Navier–Stokes equation of an incompressible stationary film flow of running back water may be written as follows in Cartesian coordinates:

$$\rho \cdot (u \cdot \nabla)u = f - \nabla P + \mu \cdot \Delta u \qquad (7)$$

where u is the water velocity in the film and f the total volumetric force on the film. Equation (7) may be expressed into local coordinates attached to the streamlines. For sake of simplicity the body is assumed to be a flat plane.

The local coordinates (s, y, r), the axes of which are defined by the vectors (i, j, k), are shown in Fig. 5 where s is the curvilinear abscissa along the wall air streamlines, y the height in the water film, and r the transverse distance from the streamline. Also shown is ω, defined as the angle on the circle locally tangential to the streamline and R the local curvature radius of the streamline

$$ds = R \cdot d\omega \qquad (8)$$

The velocity may be written

$$u = u \cdot i + v \cdot j + w \cdot k \qquad (9)$$

Equation (7) becomes, along the transverse axis r,

$$\rho\left(u\frac{\partial w}{\partial s} + v\frac{\partial w}{\partial y} + w\frac{\partial w}{\partial r} + \frac{u^2}{R} \right) = f_r - \frac{\partial P}{\partial r}$$

$$+ \mu\left(\frac{\partial^2 w}{\partial s^2} + \frac{\partial^2 w}{\partial y^2} + \frac{\partial^2 w}{\partial r^2} + \frac{2}{R}\frac{\partial u}{\partial s} - \frac{u}{R^2}\frac{\partial R}{\partial s} - \frac{w}{R^2} \right) \qquad (10)$$

Expression (10) may be simplified by ignoring the smallest terms. This may be achieved by estimating the relative magnitudes of length and velocity in the water flow. That is, u, the component of the velocity parallel to the streamlines, is much larger than the transverse components w and v; this could be false in the separated region, but it is assumed that there is no running back water in this region. Also, the water film thickness h is obviously negligible with respect to the body size C.

Then, neglecting the smallest terms of Eqs. (10) it yields

$$\rho\frac{u^2}{R} = f_r - \frac{\partial P}{\partial r} + \mu\left(\frac{\partial^2 w}{\partial y^2} + \frac{2}{R}\frac{\partial u}{\partial s} - \frac{u}{R^2}\frac{\partial R}{\partial s} \right) \qquad (11)$$

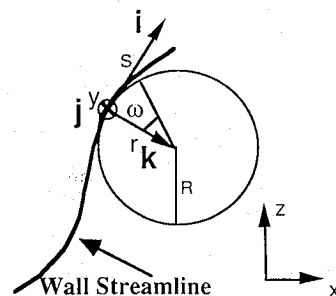Now, the mean value $\bar{w}$ of the transverse velocity w across the water thickness can be estimated.

Fig. 5 Local coordinates defined along the wall air streamlines.

Table 1 Estimation of the terms of $\bar{w}$ as a function of the velocity

Mach:	0.01	0.05	0.1	0.2	0.3	0.4	0.5	0.6
U_∞, m/s	3	15	30	60	90	120	150	180
Flow:	Laminar BL Flow						Turbulent	
$\tau 0$, Pa	0.03	0.3	1	3	5	8	44	100
$\bar{u}$, m/s	$2\ 10^{-4}$	$3\ 10^{-4}$	$6\ 10^{-3}$	$1\ 10^{-2}$	$2\ 10^{-2}$	$4\ 10^{-2}$	0.1	0.2
$hf\,[\mu]$	20	24	23	22	20	19	10	7
i	10^{-7}	10^{-7}	10^{-6}	10^{-5}	10^{-5}	10^{-5}	10^{-5}	10^{-5}
ii	10^{-2}	10^{-2}	10^{-2}	10^{-1}	10^{-1}	10^{-1}	10^{-2}	10^{-2}
iii	1	1	10^{-1}	10^{-2}	10^{-2}	10^{-2}	10^{-3}	10^{-3}
iv	10^{-2}	10^{-2}	10^{-3}	10^{-4}	10^{-4}	10^{-4}	10^{-5}	10^{-5}
v				10^{-8}				
vi				10^{-10}				

The main flow along the streamlines is assumed to be a Couette flow, and the transverse flow is assumed to have second-order polynomial form. Using boundary conditions no slip at the wall and shear stress continuity the water speed for the main flow may be expressed as

$$u(y) = b \cdot y \qquad (12)$$

and for the transverse flow

$$w(y) = -a \cdot hf \cdot y + a \cdot y^2 \qquad (13)$$

Equation (11) can be integrated across the water film thickness assuming the volumetric forces are constant across the film thickness:

$$\frac{\rho b^2 hf^3}{3R} = f_r \cdot hf - \rho \cdot g \cdot hf + 2\mu \cdot hf \cdot a$$
$$+ \mu \frac{hf^2}{R} \frac{\partial b}{\partial s} - \mu \frac{b \cdot hf^2}{2R^2} \frac{\partial R}{\partial s} \qquad (14)$$

An expression of a is derived from Eq. (14)

$$a = \frac{\rho b^2 hf^2}{6R\mu} - \frac{fr}{2\mu} + \frac{\rho g}{2\mu} \frac{\partial hf}{\partial r} - \frac{hf}{2R} \frac{\partial b}{\partial s} + \frac{b \cdot hf}{4R^2} \frac{\partial R}{\partial s} \qquad (15)$$

and b is derived from the integration of u across the film thickness, Eq. (12):

$$b = 2\bar{u}/hf \qquad (16)$$

The partial derivative of Eq. (16) gives

$$\frac{\partial b}{\partial s} = -\frac{2\bar{u}}{hf^2} \frac{\partial hf}{\partial s} \qquad (17)$$

Integrating Eq. (13) gives the mean value of w:

$$\bar{w} = \frac{1}{hf} \int_{y=0}^{y=hf} (-a \cdot hf \cdot y + a \cdot y^2)\, dy = -\tfrac{1}{6} a hf^2 \qquad (18)$$

Then w is expressed as

$$\bar{w} = \bar{u} \left(-\frac{\rho \bar{u} hf^2}{9R\mu} + \frac{fr hf^2}{12\mu \bar{u}} \right.$$
$$\left. -\frac{\rho \cdot g \cdot hf^2}{12\mu \bar{u}} \frac{\partial hf}{\partial r} + \frac{hf}{6R} \frac{\partial hf}{\partial s} - \frac{hf^2}{12R^2} \frac{\partial R}{\partial s} \right) \qquad (19)$$

Estimation of the Volumetric Forces

The transverse component f_r of the total volumetric force f may be estimated. In the present case the volumetric forces are, on one hand, the gravity force f_g and, on the other hand, the droplet impact f_i due to the kinetic energy variation of the impacting droplets cloud. Newton's second law enables the impact force to be approximated as

$$F_i \approx \frac{\Delta p}{\Delta t} \approx LWC \cdot \beta \cdot U_\infty \cdot ds \cdot dr \cdot U_i \qquad (20)$$

where F_i is the impact force, p the linear momentum of droplets, and U_i the droplet impact velocity; $ds \cdot dr$ is the wall surface element.

Assuming the impact force is uniform across the film thickness, the volumetric impact force is derived:

$$f_i = \frac{F_i}{ds \cdot dr \cdot hf} \approx \frac{LWC \cdot \beta \cdot U_\infty}{hf} U_i \qquad (21)$$

The upper limit of f_r, the component of $f_i + f_g$ along the r direction, is

$$f_r \leq \frac{LWC \cdot \beta \cdot U_\infty^2}{hf} + \rho \cdot g \qquad (22)$$

Rewriting Eq. (19)

$$\bar{w} = \bar{u} \left(\underbrace{-\frac{\rho \bar{u} hf^2}{9R\mu}}_{i} + \underbrace{\frac{LWC \cdot \beta \cdot U_\infty^2 hf}{12\mu \bar{u}}}_{ii} + \underbrace{\frac{\rho \cdot g \cdot hf^2}{12\mu \bar{u}}}_{iii} \right.$$

$$\left. \underbrace{-\frac{\rho \cdot g \cdot hf^2}{12\mu \bar{u}} \frac{\partial hf}{\partial r}}_{iv} + \underbrace{\frac{hf}{6R} \frac{\partial hf}{\partial s}}_{v} - \underbrace{\frac{hf^2}{12R^2} \frac{\partial R}{\partial s}}_{vi} \right) \qquad (23)$$

Order of Magnitude of the $\bar{w}$ Terms

The importance of $\bar{w}$ with respect to $\bar{u}$ may be evaluated by calculating the terms in Eq. (23). However some variables in Eq. (23) cannot be expressed analytically as functions of the freestream conditions; $\bar{u}$ and hf are such variables.

To quantify the order of magnitude of these variables a simulation was run on a two-dimensional NACA0012 airfoil with a 0.25-m chord. The two-dimensional icing code was modified to perform the simulation of the runback as a Couette flow. Freestream conditions were $LWC = 1.5$ g/m^3, $3 < U_\infty < 180$ m/s, and $T_\infty > 0°$C to avoid icing.

Thus the approximate deviation of the film flow with respect to the wall air streamlines may be estimated as shown in Table 1. From the table it is apparent that, the centripetal force i, the effect of pressure gradient due to transverse variation of film thickness iv, the effect of longitudinal variation of the film thickness along curved streamlines v, and the effect of streamlines curvature variation vi are negligible whatever the flight speed is. Deviation due to impact forces ii is negligible, except if droplets trajectories are perpendicular to runback flow and parallel to the wall (maximum deviation = 5 deg). Gravity force iii cannot be neglected for low speed ($M_\infty \leq 0, 1$) near stagnation line. Hence, the conclusion is that for usual flight conditions the runback paths closely follow the wall air streamlines.

Thermodynamic Grid Creation

To simplify the thermodynamic balance a new body grid is created along the runback paths; this grid is called thermodynamic grid. Using this grid, one can establish the thermodynamic balance nearly in the same way as is done in a two-dimensional model. In this new grid there is no runback across lateral grid edges (Fig. 6).
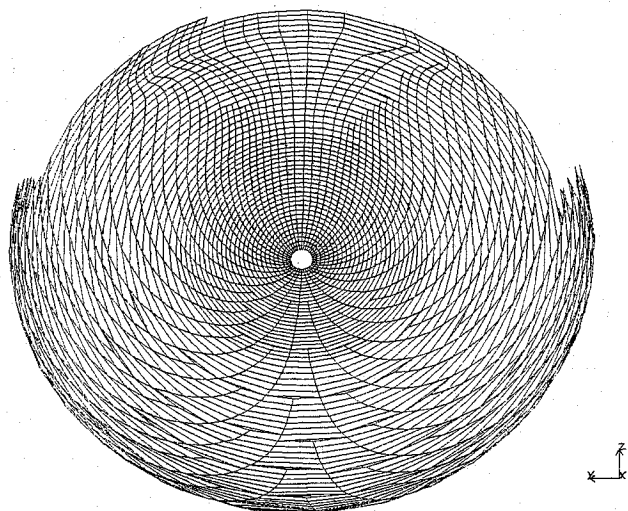
Fig. 6   Thermodynamic grid built along the runback paths on an ellipsoid.

Fig. 7   To maintain a quasiconstant cell width runback paths lines may disappear or appear, running back water is mixed or split.

Heat and Mass Balance

The heat and mass balance is established along the runback paths in the thermodynamic grid. It uses the classical Messinger equations[9] except for the evaporation term which is improved using Jakob's formulation.[10] When there is a temperature gradient through the boundary layer thickness, evaporation depends not on water vapor concentration gradient but on water vapor partial pressure gradient.[10]

Noting that vapor partial pressure at the top of boundary layer is the same as in the freestream, the evaporation flux may be expressed as

$$\dot{m}_{vap} \cong \left(\frac{1}{Le}\right)^{\frac{2}{3}} \frac{h}{Cp_{air}} \frac{M_{m(water)}}{M_{m(air)}} \frac{T_\infty}{\bar{T}} \frac{P_{vs_{wall}} - P_{vs_\infty}}{P_\infty}$$

where $\bar{T} = (T_W + T_\infty)/2$ is a mean temperature.

The thermodynamic balance gives the ice growth rate at the center of each panel of the thermodynamic grid.

Three-Dimensional Effects

It is necessary to add a cell surface correction to take into account the divergence or convergence of the runback due to three-dimensional effects (Fig. 7). The usual correction when the flow goes from one cell down to another one is as follows:

$$\dot{m}_i^{in} = \dot{m}_{i-1}^{out} \cdot (S_{i-1}/S_i)$$

where $i - 1$ and i are the indices of the grid cell along runback, S_i is the surface of cell i, $\dot{m}_i^{in}$ is the mass flow running in per unit area of cell i and $\dot{m}_{i-1}^{out}$ is the mass flow running out per unit area of cell $i - 1$.

One or more runback lines may disappear or appear to keep the cell size within a given range; when one or more lines disappear, the flow from two or more cells is mixed into one cell conserving heat and mass (Fig. 7):

$$\dot{m}_i^{in} = \dot{m}_{i-1}^{out} \cdot (S_{i-1}/S_i)$$

Conversely, when one or more lines appear, the flow from one cell is split between the children cells. Each child cell receives a flow that is proportional to the length of the edge common with the parent cell (Fig. 7):

The runback flux and ice accretion rate are calculated for each cell. Then a one time step ice shape may be derived.

Iced Body Grid

The ice shape is simulated by a deformation of the grid (Fig. 8), it may be either the new grid made along the runback direction or,
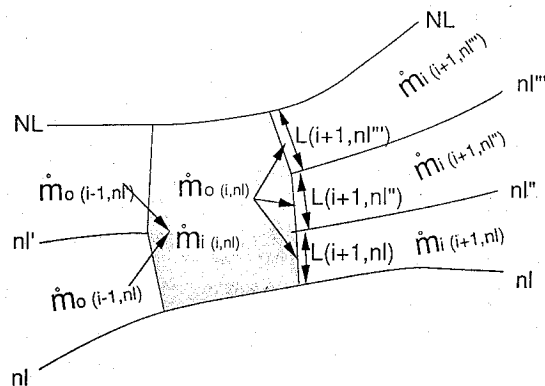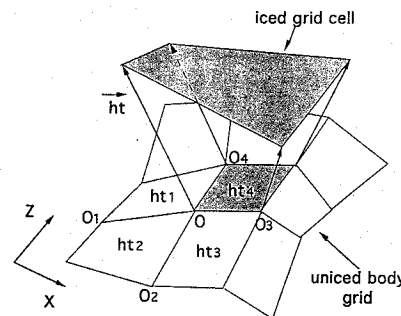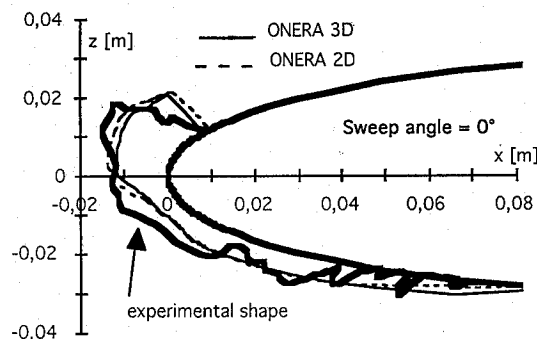

Fig. 8   Generation of the iced grid.

Fig. 9   One time step ice shape, NACA 0012 airfoil, 0.53-m chord, $\alpha = 4$ deg, $T_\infty = 266.45$ K, $P_\infty = 95.61$ kPa, Mach $= 0.177$, $LWC = 1.3 \ 10^{-3}$ Kg/m^3, 480-s icing time, 20-μm droplet diameter.

by interpolating the icing rate, the original grid. The deformation of the original grid allows one to re-inject it in the icing code and to perform a multistepping ice growth.

The ice height ht_i on each cell is calculated as follows: $ht_i =$ icing-rate $*$ icing-time. This calculation takes into account the curvature of the profile; as the cell surface increases (or decreases depending on the curvature) with the ice deposit, its collection efficiency increases (or decreases) proportionally. It is valid as long as the local catch efficiency is not modified much by the ice shape influence.

The deformation of the grid is achieved by moving each node along the normal vector n at the body surface. The displacement length $|ht|$ is the average ice height on the cells sharing the node, between 1 and 4 (Fig. 8). That is,

$$n = (O_1 - O_3) \otimes (O_2 - O_4)$$

the node's normal vector, where O_i is an edge vector going from node O to node O_i and $ht = \sum ht_i/4 \cdot n/|n|$ the node displacement vector.
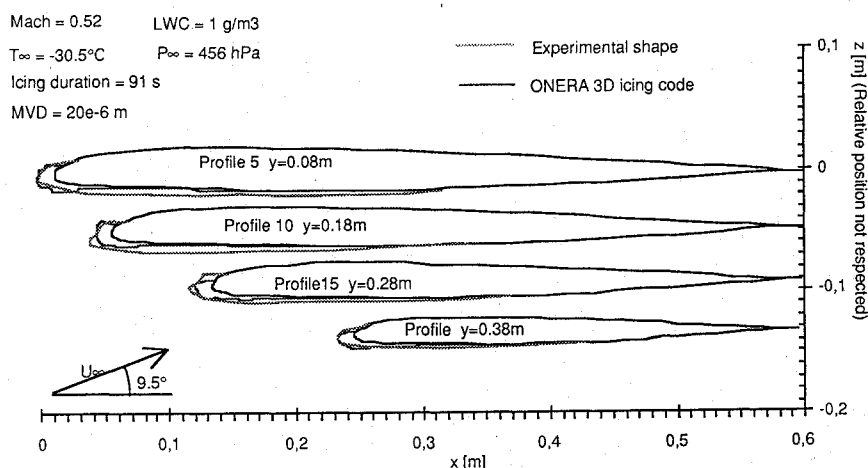
Fig. 10 Ice shape calculated by the three-dimensional icing code and compared with the experimental shape.

Domain of Validity and Limitations

From the hypothesis used for each step of the model development, a theoretical domain of validity for the ONERA three-dimensional icing code may be deduced.

The use of an Euler method for solving the inviscid flow extends the domain of validity up to transonic flows. Nonetheless, the validity of such a method still restricts its use to low incidence and well-profiled bodies. This is due to the lack of viscous coupling that prevents one from taking into account boundary-layer separation.

The validity of the rough wall boundary-layer calculation was demonstrated on cylinders[1] by comparing with Achenbach[11] and Van Fossen experiments. The precision of the heat transfer estimation decreases more slowly than the Makkonen[12] model used in two-dimensional icing codes as the Reynolds number and the roughness increase.

The runback paths integration is valid as long as the gravity effects are negligible, that is, when the body speed is more than about Mach 0.1.

The thermodynamic balance does not add any limitation of validity. But there is a small amount of uncertainty due to the sharing between evaporating and sublimating surfaces. One applies evaporation on the whole surface of a cell as long as there is runback and sublimation when all the impinging water freezes at once. Rivulet formation is ignored.

Comparison with Experimental Data

Comparison with Experimental Two-Dimensional Shapes

Some comparisons were performed on a two-dimensional experimental shape between two-dimensional and three-dimensional codes. It was not planned to validate the three-dimensional model using two-dimensional shape but only to check whether the results were at least as good as those yielded by the two-dimensional icing code.

The three-dimensional icing code was applied to the NACA 0012 airfoil with a 1-m span. The results are given at midspan where two-dimensional conditions are very closely achieved.

One can see in Fig. 9 that the two-dimensional and three-dimensional icing codes give the same shape with the one time step calculation. Compared with the experimental shape the result is good.

Comparison with an Experimental Three-dimensional Ice Shape on a Rotor Blade Tip

The three-dimensional code was used on a rotor blade tip with fully three-dimensional characteristics. From the base to the top along the span, the chord varies from 0.6 to 0.2 m, the leading-edge sweep angle starts at 0 and ends at 60 deg. The trailing edge is perpendicular to the flow and is lightly spun so that the incidence angle at the top is 0.74 deg less than at the base. The span is 0.48 m. The rotor blade tip is built on a NACA 13106 profile, which means that it is very thin (6% of the chord). The comparison (see Fig. 10)
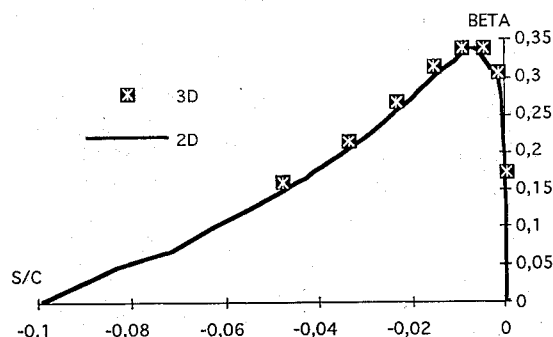

Fig. 11 Catch efficiency with three-dimensional code and two-dimensional corrected code, NACA 0012 airfoil, 0.53-m chord, α = 4 deg, T_∞ = 266.45 K, P_∞ = 95.61 kPa, Mach = 0.177, 60-deg sweep angle, and 20-μm droplet diameter.

between the three-dimensional simulated ice shape and the experimental one on a rotor blade tip shows the good performance of the three-dimensional icing code.

Sweep Effect on an Infinite Wing

To evaluate the possibilities of doing ice prediction on a infinite swept wing with the two-dimensional icing code, the three-dimensional icing code was run on a 60-deg swept wing. The local catch efficiency is calculated by the two-dimensional code using the correction proposed by Dorsch and Brun[13] for swept wings; that is,

$x \rightarrow x \cdot \cos(\phi)$ x coordinate

$z \rightarrow z$ z coordinate

$U_\infty \rightarrow U_\infty \cdot \cos(\phi)$ freestream velocity

$\beta \rightarrow \beta \cdot \cos(\phi)$ catch efficiency

$c \rightarrow c \cdot \cos(\phi)$ chord

$\alpha \rightarrow \alpha/\cos(\phi)$ angle of attack

The two-dimensional icing code was run using the same Dorsch and Brun[3] correction in the local efficiency calculation and using the speed correction [i.e., $U_\infty = U_\infty \cdot \cos(\phi)$] in the other parts of the code.

The local efficiency values obtained using the three-dimensional code were compared to the ones obtained with the two-dimensional corrected code. As one can see in Fig. 11 the same values are found in both cases. A two-dimensional code can then be used to determine the catch limits on a yanked profile.

Then, ice shape prediction was performed with the two codes and compared the fully three-dimensional calculation and the corrected two-dimensional calculation.

Since the two-dimensional icing code does not take into account the lateral component of the airflow, the total speed at the stagnation line will still be zero instead of $U \cdot \sin(\phi)$ as in the three-dimensional
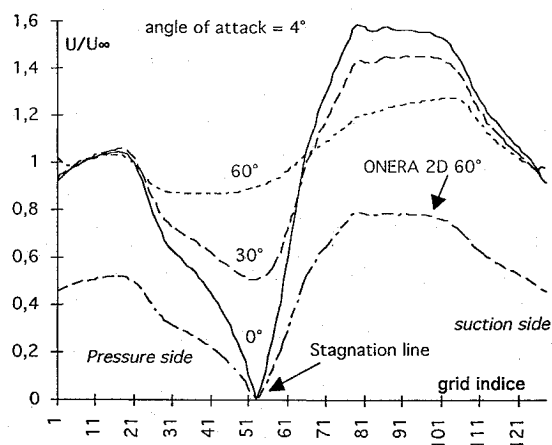
Fig. 12   Air flow along the profile with the sweep angle calculated by ONERA three-dimensional model.
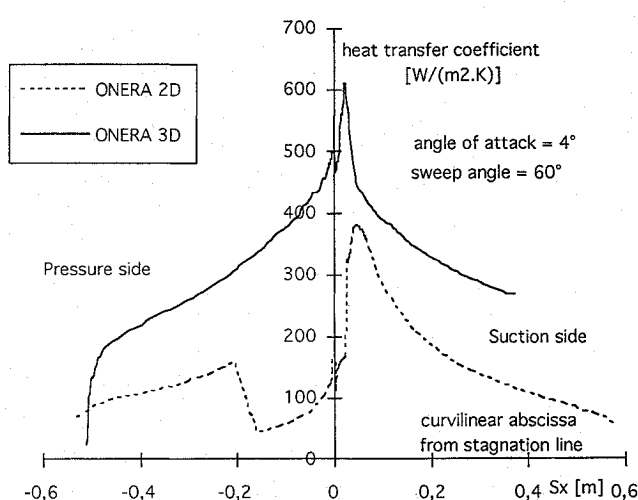

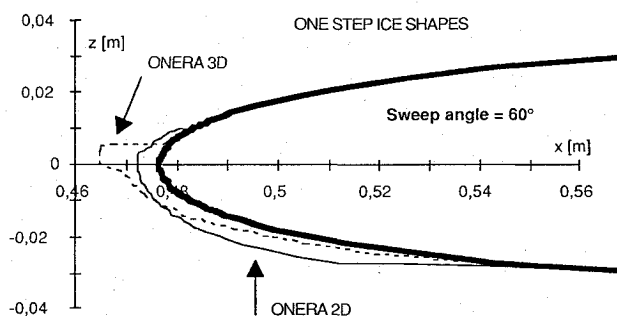Fig. 13   Heat transfer on a 60-deg swept wing.

Fig. 14   Ice shapes on swept wing ONERA three-dimensional and corrected ONERA two-dimensional code, air flow by ONERA two-dimensional code at 60 deg of sweep.

model (Fig. 12). As the heat transfer coefficient depends on total speed, it will be underestimated in the two-dimensional model. In other hand, the relative velocity variation is overestimated, and the heat transfer distribution is not the same in both cases (Fig. 13). This can smooth the ice accretion, and the ice shape is more aerodynamic and, therefore, the aerodynamic losses will be underestimated or it will produce unrealistic horns (Fig. 14), depending on the ice conditions.

The differences observed between the two- and three-dimensional models on the ice shapes are very large; until a correct value for the heat transfer coefficient value calculated with two-dimensional code on swept wing is obtained, the results need to be carefully analyzed to determine if the shapes are conservative.
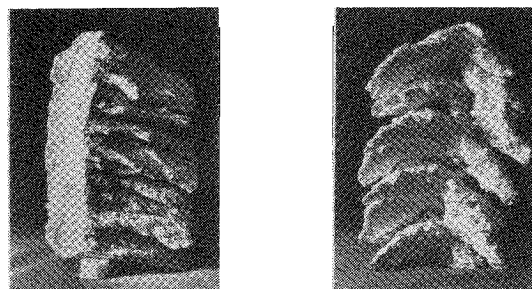

Fig. 15   Example of lobster tail ice shape on a swept wing, plaster cast, photographed by J. J. Begot; left picture taken from below the wing; right picture upstream view.
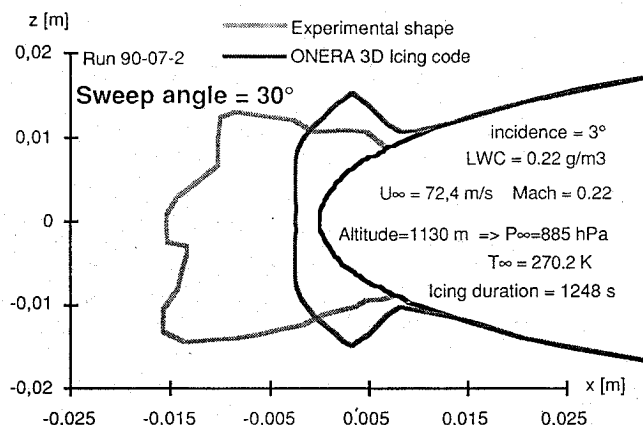

Fig. 16   Comparison of an experimental lobster tail envelope shape with the shape predicted through the three-dimensional icing code.

Lobster Tail Ice Shapes: Limit of the Continuum Flux Approach

No icing model takes into account microphysical features. Actually, all of them consider the impinging supercooled water to be a continuum. In three-dimensional cases, shadow effects due to the impact and the individual freezing of supercooled droplets[2] may give rise to shapes known as "lobster tails"[14] (Fig. 15). In that case, the simulated shapes are quite underestimated (Fig. 16).

The effect of a lobster tail growth is to increase the volume of deposit ice as the filling ratio is not equal to 1. The differences between experimental and calculated shapes are too large, and so a study was undertaken to analyze and model the mechanisms possibly involved in lobster tail growth described in Ref. 2.

Conclusion

The ONERA three-dimensional icing code was described. A three-dimensional compressible Euler method is used for calculating the inviscid compressible flow even with transonic flight conditions; this method allows a fast droplet trajectory calculation. The creation of a new grid adapted to boundary-layer calculation enables a better approximation of convection heat transfer nearby the stagnation line (or stagnation point). The running back water is shown to follow quite well the air wall stream lines for usual flight conditions (Mach > 0.1). A new grid is built along these runback paths, which enable an easy establishment of the thermodynamic balance. Hence, ice deposit height is calculated, and a grid of the iced body is created which may be used for multistepping ice growth calculation. Comparisons of the three-dimensional code with the two-dimensional one and with experimental shapes of uniform ice deposit exhibit a very good agreement. From the comparison of the sweep corrected two-dimensional code with the fully three-dimensional one on a swept wing, it is clear that the corrected two-dimensional code can predict the local catch efficiency but not the ice shape on swept wings. Finally, it is shown that the three-dimensional icing model in its present state cannot simulate lobster tail ice shapes.

References

[1]Hedde, T., and Guffond, D., "Development of a Three-Dimensional Icing Code, Comparison with Experimental Shapes," AIAA Paper 92-0041, Jan. 1992.

[2]Hedde, T., and Guffond, D., "Improvement of the ONERA 3-D Icing Code, Comparison with 3-D Experimental Shapes," AIAA Paper 93-0169, Jan. 1993.

[3]Guffond, D., Hedde, T., and Henry, R., "Overview of Icing Research at ONERA," AGARD/FDP Joint International Conf. on Aircraft Flight Safety—Actual Problems of Aircraft Development, Zhukovsky, Russia, 1993, pp. 122,128.

[4]Arnal, D., Coustols, E., and Juillen, J. C., "Etude expérimentale et théorique de la transition sur une aile en flèche infine," *La Recherche Aérospatiale*, Vol. 4, 1984, pp. 275–290.

[5]Van Driest, E. R., "On Turbulent Flow Near a Wall," *Journal of the Aeronautical Sciences*, Vol. 23, No, 11, 1956, pp. 1007–1036.

[6]Michel, R., Quemard, C., and Durant, R., "Application d'un schéma de longueur de mélange à l'étude des couches limites turbulentes d'équilibre," ONERA-NT 154, 1969.

[7]Yamaguchi, K., and Hansman, R. J., "Heat Transfer on Accreting Ice Surfaces," AIAA Paper 90-0200, Jan. 1990.

[8]Hansman, R. J., "Analysis of Surface Roughness Generation in Aircraft Ice Accretion," AIAA Paper 92-0298, Jan. 1992.

[9]Messinger, B. L., "Equilibrium Temperature of Unheated Icing Surface as a Function of Airspeed," *Journal of the Aeronautical Sciences*, Vol. 20, No. 1, 1953, p. 29.

[10]Jakob, M., *Heat Transfer*, Vol. 1, Wiley, New York, pp. 588–605.

[11]Achenbach, E., "The Effect of Surface Roughness on the Heat Transfer from a Circular Cylinder," *Journal of Heat and Mass Transfer*, Vol. 20, 1977, pp. 359–369.

[12]Makkonen, L., "Heat Transfer and Icing of a Rough Cylinder," *Journal of Cold Region Science and Technology*, Vol. 10, 1985, pp. 105–116.

[13]Dorsch, R. G., and Brun, R. J., "A Method for Determining Cloud Droplet Impingement on Swept Wings," NACA TM 293, April 1953.

[14]Reehorst, A. L., "Prediction of Accretion on a Swept NACA 0012 Airfoil and Comparisons to Flight Test Results," AIAA Paper 92-0004, Jan. 1992.